

Theoretical Study on Horizontal-Type SAW Device with Dual Function of Sensing and Removal of Non-specific Binding

C. CHEN^a, Y. WANG^{b,*}, T. AO^a AND G. HUI^a

^aYunnan Normal University, No.1 Yuhua area, Chenggong District, 650500, Kunming, Yunnan Province, China

^bChangchun University of Science and Technology, No. 7089 Weixing Road, Changchun 130022, Changchun, Jilin Province, China

Received: 21.10.2023 & Accepted: 18.01.2024

Doi: [10.12693/APhysPolA.145.281](https://doi.org/10.12693/APhysPolA.145.281)

*e-mail: Wangyuting0119@163.com

In this paper, a horizontal-type surface acoustic wave device based on electrode width control interdigital transducer/polymethylmethacrylate/54° Y–X LiNbO₃ is proposed to achieve the removal of non-specific binding particles by Rayleigh waves and the detection of meningococcus by Love waves. It is proved that the surface acoustic wave force plays a leading role in the removal of non-specific binding, and the frequency of the acoustic wave also affects the removal effect. The advantage of electrode width control interdigital transducer lies not only in overcoming the shortcomings of bidirectional and focused interdigital transducers, but also in improving the utilization of acoustic waves and the sensitivity of the sensor. When non-specific binding particles are removed by Rayleigh waves, the Love wave sensor shows a sensitivity of 330 Hz/(ng/TL) and a detection limit of 50 pg/μL for meningococcus.

topics: surface acoustic wave (SAW) force, acoustic radiation force, Rayleigh and Love waves, electrode width control interdigital transducer

1. Introduction

Technological advances in biosensor development in recent years have made it possible to produce extremely fast and highly responsive biosensors [1]. The biosensors are generally classified into four major categories according to the detection principles: electrochemical, thermal, optical, and acoustic. They have been extensively studied and put into practical applications [2]. M. Tak et al. [3] and R. Gupta et al. [4] use the electrochemical method to detect bacterial viruses. K. Gracie [5] and M.T. Yarakı et al. [6] use surface-enhanced Raman spectroscopy (SERS) technology to detect and quantify biological samples. G. Kaur et al. [7] and A. Ramola et al. [8] respectively report the detections of cancer cells and meningococci using the surface plasmon resonance (SPR) method. In addition, there are some studies reporting the use of polymerase chain reaction to detect biological samples [9–14]. However, these techniques have limitations that make them unsuitable for wireless sensing applications, which could pave the way for implantable devices to be used in a variety of diagnostic and health monitoring applications. Acoustic-based devices are well suited for biosensing applications due to their stable fundamental frequency, ease of analyzing the output, and wireless

integration. Furthermore, acoustic biosensors have significant advantages in surface modifications as they are more customizable to the detection region, thus allowing the detection of different samples, such as proteins, enzymes, DNA, etc. [15]. H. Oh et al. [16] use a wireless Love wave biosensor for simultaneous detection of multiple biomolecules. D.W. Branch et al. [17] achieved low-level detection of *Bacillus anthracis* simulants using Love-wave biosensors. S.M. Li et al. [18] completed the precise measurement of carcinoembryonic antigen based on the Love wave biosensor. J. Ji et al. [19] achieved specific detection of *Staphylococcus aureus* gene sequences using single-layered graphene/Au-nanoparticles-based Love wave biosensors. H. Wu et al. [20] use a Love wave biosensor to monitor the adhesion process of tendon stem cells. W. Wei et al. [21] study a polyethylene polymer-based SAW Lamb device for the detection of serum pepsinogen. M. Bharati et al. [22] use a Lamb wave resonator to efficiently detect *Neisseria meningitidis* and study the effects of symmetric and anti-symmetric modes of Lamb waves on detection. J. Nam et al. [23] reported a Lamb wave-based device for detecting gene amplification through the rolling circle amplification process. Although the Lamb wave sensor has high mass sensitivity, it is not suitable for liquid sensing, which restricts its development in the

field of biosensing. By comparison, Love mode surface acoustic wave (SAW) with only one component of mechanical displacement parallel to the substrate surface and perpendicular to the propagation direction provides low damping in a liquid, which is why Love mode SAW sensor is widely used in various biosensing applications due to its suitability for liquid sensing and high sensitivity. In this paper, a Love wave-based biosensor for the detection of DNA is proposed. Meningococcus has been chosen for theoretical study because its early detection is critical to controlling its spread and saving lives in time.

SAW biosensors suffer from the problem of non-specific binding (NSB) protein on the surface of the device [24, 25]. Due to the presence of NSB particles, the detection results are inaccurate. It is shown that the Rayleigh wave mode with a surface normal component couples strongly to the fluid and radiates longitudinal waves into the fluid. Because of the viscous dissipation of fluid, the pressure gradient exists in the propagation direction of the longitudinal wave [26], which causes the acoustic streaming phenomenon. The acoustic streaming exerts steady viscous stresses on the boundary layer. Although the value of viscous stresses is small, it is enough to remove the NSB on the biosensor surface [27]. S.K.R.S. Sankaranarayanan and R. Singh [28] analyzed the main mechanism of the removal of NSB by acoustic streaming in detail and verified the removal effect of the designed SAW devices by experiments and finite element calculation. Later, S.K.R.S. Sankaranarayanan [25] replaced the traditional bidirectional interdigital transducer (IDT) with a focused IDT which focuses the acoustic waves in the removal region, greatly increases the intensity of the acoustic waves, and improves the removal efficiency of NSB. However, the fabrication of focused IDT is more difficult, and SAW must be focused on the removal region. In this paper, electrode width control (EWC) IDT is proposed to solve the problems.

S.M. Li and V.R. Bhethanabotla [29] place two pairs of orthogonal IDTs on ST quartz substrates, which excite Rayleigh waves and horizontal shear waves, respectively. Although this device can both detect biomarkers and remove NSB particles, the propagation directions of Rayleigh waves and horizontal shear waves in the device are orthogonal (hence the term orthogonal-type SAW device). The orthogonal placement of IDTs increases not only the number of IDTs but also the size of the sensor. In addition, the Rayleigh wave and the horizontal shear wave work at the same time; when the NSB is removed by the SAW force and the acoustic radiation force induced by Rayleigh waves, the mass loading effect of the biological sample is also weakened because the samples also experience the SAW force and the acoustic radiation force. As a result, the developed sensor based on the horizontal shear wave does not accurately detect the biological sam-

ple. But for the $54^\circ Y-X$ LiNbO₃ substrate, when a pair of IDTs are placed horizontally on the substrate surface, it can, respectively, excite Rayleigh waves and horizontal shear waves at specific frequencies, and the propagation directions of the two acoustic waves are parallel. Furthermore, LiNbO₃ piezoelectric material has high electromechanical coupling coefficient (up to 9%) and piezoelectric constants ($d_{15} = 68$ pC/N, $d_{33} = 6$ pC/N, $d_{22} = 22$ pC/N, $d_{31} = -1$ pC/N) [30, 31]. The piezoelectric material with a higher electromechanical coupling coefficient provides a more effective conversion between electrical energy and mechanical energy, enabling larger power density and wider bandwidth. Piezoelectric constants reflect the material sensitivity of the piezoelectric effect. In sensor applications, higher piezoelectric constants enable the generated signal to be detected more easily. Therefore, a SAW device with both sensing and removal functions prepared on the $54^\circ Y-X$ LiNbO₃ substrate (referred to as a horizontal-type SAW device) is proposed in the paper. In order to achieve the Love wave, the waveguide layer with lower shear velocity compared to the substrate must be placed on the piezoelectric substrate. Polymethyl methacrylate (PMMA) is selected because of its good physical/chemical resistance in aqueous or harsh environments and strong bonding to $54^\circ Y-X$ LiNbO₃ substrate.

In this paper, we propose a horizontal-type SAW device based on EWC IDT/PMMA/ $54^\circ Y-X$ LiNbO₃ to achieve the removal of NSB particles and the detection of meningococcus. Compared with the existing studies, the innovative works of this paper are as follows. Firstly, the role of acoustic radiation force in the process of removing NSB particles is analyzed, and the effects of acoustic frequency and mechanical properties of NSB particles on acoustic radiation force are studied. Secondly, EWC IDT is applied to the removal of NSB particles and the detection of meningococcus; this not only overcomes the shortcomings of bidirectional and focused IDTs, but also improves the utilization of acoustic waves and the sensitivity of the sensor. Finally, the influences of waveguide layer thicknesses on the Love wave propagation and insertion loss of devices are studied, and the optimal thickness is determined. Also, the mass sensitivity and detection limit of the horizontal-type SAW device for meningococcus are calculated.

2. Traveling SAW systems and control equations

2.1. Traveling SAW device for the detection of meningococcus and the removal of NSB particles

The proposed SAW removal and biological detection device is shown in Fig. 1a. It consists of a piezoelectric substrate, EWC IDTs, a waveguide layer, and detection channels. The piezoelectric substrate is $54^\circ Y-X$ LiNbO₃, 5 mm long, 2.4 mm wide,

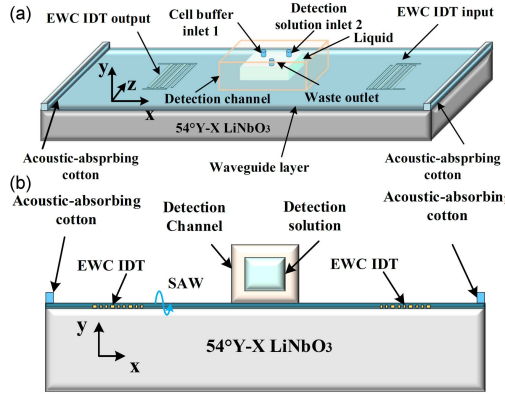


Fig. 1. Horizontal-type SAW device with dual function of sensing and removal of non-specific binding. (b) Plane view of horizontal-type SAW device in y - x direction.

and $200 \mu\text{m}$ thick. The waveguide layer overlaying the upper surface of the substrate is PMMA material, 5 mm long, 2.4 mm wide, and $3 \mu\text{m}$ thick. A pair of EWC IDTs with a period of $37 \mu\text{m}$ are placed on the interface between the waveguide and the substrate and used to generate high-frequency SAW. The acoustic absorption layers are placed at both ends of the substrate to reduce the reflection of acoustic waves from the boundary. The detection channel is made of polydimethylsiloxane (PDMS) material and is $110 \mu\text{m}$ long, $200 \mu\text{m}$ wide, and $50 \mu\text{m}$ high, and contains two inlets and one outlet. The phosphate-buffered saline (PBS) and meningococcal oligonucleotide solution are injected into the two inlets, respectively (the two inlets do not work at the same time). The inner bottom of the PDMS channel contains a biologically sensitive layer, which is modified with complementary DNA probes. Meningitidis oligonucleotides bind specifically to complementary DNA probes.

The detection of meningococcal oligonucleotides is mainly divided into three processes:

- (i) PBS buffer solution is pumped into the channel from inlet 1. After it fills the channel, the outlet and inlet 1 are closed, and the frequency f_1 of the SAW device is measured. Then, open the waste outlet and drain the PBS buffer solution from it.
- (ii) meningococcal oligonucleotide solutions are pumped into the channel through inlet 2 and bind specifically to complementary DNA probes. Then, the Rayleigh wave is excited to remove NSB particles. The removed NSB particles are discharged from the outlet.
- (iii) PBS solution is pumped into the channel from inlet 1. After it fills the channel, the outlet and inlet 1 are closed, and the frequency f_2 of the device is measured. The difference between the f_1 and f_2 is the result of specific binding of meningococcal oligonucleotides. The purpose of detecting meningococcus is achieved.

The feasibility of the proposed experimental scheme can be confirmed based on similar previous studies. Experimental studies by S.K.R.S. Sankaranarayanan et al. [25] have shown the applicability of Rayleigh wave modes to remove non-specific binding proteins from the surfaces of SAW devices. The fluorescently labeled sample of bovine serum albumin (BSA) is placed on a fluorescent microscope for intensity measurements. The reduction of intensity indicates a significant reduction of the non-specific binding BSA.

In the process of removing NSB by Rayleigh waves, SAW will be strongly coupled with the fluid. It is necessary to calculate the interaction between the fluid and the acoustic wave. If the three-dimensional model shown in Fig. 1a is used for calculation, a huge amount of calculation is required. It is also used when calculating the Love wave sensing. Note that the Love wave has a displacement component in the z direction, which must be considered.

2.2. Control equations for the fluid domain

The laws of conservation of mass and momentum govern the motion of viscous compressible fluids and can be described as [32, 33]

$$\frac{\partial \rho}{\partial t} + \nabla \cdot (\rho \mathbf{v}) = 0, \quad (1)$$

$$\rho \frac{\partial \mathbf{v}}{\partial t} + \rho (\mathbf{v} \cdot \nabla) \mathbf{v} = -\nabla p + \mu \nabla^2 \mathbf{v} + \left(\mu_b + \frac{\mu}{3} \right) \nabla (\nabla \cdot \mathbf{v}), \quad (2)$$

where ρ is the density of the fluid, \mathbf{v} is the fluid velocity, p is the fluid pressure, and μ and μ_b are the shear viscosity and bulk viscosity, respectively. Here, ρ , p , and \mathbf{v} are understood to be in Euler form [34] and are functions of time t and spatial position r in a fixed volume. Fluid pressure, acoustic velocity, and fluid density satisfy

$$p = c_0^2 \rho, \quad (3)$$

which can be used to describe the motion of fluid more conveniently. In (3), c_0 is the acoustic velocity of the fluid at rest. By combining (1)–(3) with appropriate boundary conditions, the state of acoustic waves in fluids can be completely determined. Due to the time difference between acoustic oscillations and particle motion [35], the fluid motion induced by harmonics can be divided into two parts: a periodic component with the same period of acoustic driving and a second-order component with a non-zero time average. Using the Nyborg perturbation method, the fluid velocity, pressure, and density can be written as the following expressions [36]

$$p = p_0 + p_1 + p_2, \quad (4)$$

$$\mathbf{v} = \mathbf{v}_0 + \mathbf{v}_1 + \mathbf{v}_2, \quad (5)$$

$$\rho = \rho_0 + \rho_1 + \rho_2, \quad (6)$$

where subscripts “0”, “1”, and “2” represent zero-order, first-order, and second-order components, respectively.

Ignoring the high-order terms of (4)–(6), the first-order equations can be derived. Their form is the following

$$\frac{\partial \rho_1}{\partial t} + \rho_0(\nabla \cdot \mathbf{v}_1) = 0, \quad (7)$$

$$\rho_0 \frac{\partial \mathbf{v}_1}{\partial t} = -\nabla p_1 + \mu \nabla^2 \mathbf{v}_1 + \left(\mu_b + \frac{\mu}{3}\right) \nabla(\nabla \cdot \mathbf{v}_1), \quad (8)$$

where μ_b and μ are the bulk and shear viscosities of the fluid, respectively. In the same way, time-averaged second-order equations can be written as

$$\left\langle \frac{\partial \rho_2}{\partial t} \right\rangle + \rho_0 \nabla \cdot \langle \mathbf{v}_2 \rangle = -\nabla \cdot \langle \rho_1 \mathbf{v}_1 \rangle, \quad (9)$$

$$\rho_0 \left\langle \frac{\partial \mathbf{v}_1}{\partial t} \right\rangle + \left\langle \rho_1 \frac{\partial \mathbf{v}_1}{\partial t} \right\rangle + \rho_0 \langle \mathbf{v}_1 \cdot \nabla \mathbf{v}_1 \rangle - \nabla \langle p_2 \rangle + \mu \nabla^2 \langle \mathbf{v}_2 \rangle + \left(\mu_b + \frac{\mu}{3}\right) \nabla(\nabla \cdot \langle \mathbf{v}_2 \rangle), \quad (10)$$

where $\langle A \rangle$ denotes the time average of the quantity A over one oscillation period.

As J.T. Stuart [37] points out, the inertia term in (10) is important and must be retained in the equation. Furthermore, the attenuations of acoustic waves inside the viscous boundary layer (the thickness of the viscous boundary layer is $d = \sqrt{2\mu/(\rho_0\omega)}$, and ω is the angular frequency of the incident acoustic wave) as well as in other regions are considered, so the last term in (5) related to the bulk viscosity must also be retained. It can be seen from the control equations of the first- and second-order fields that the second-order field is generated by the first-order field as the source term. The strength of the first-order field determines the strength of the second-order field.

2.3. Numerical realization

The detections of meningococci and the removal of NSB shown in Fig. 1a are not performed simultaneously. Therefore, the simulation is divided into two parts: one is to calculate the removal of NSB by the Rayleigh wave, and the other is to calculate the detections of meningococcus by the Love wave. The Rayleigh wave is strongly coupled with the fluid, which will cause the acoustic streaming phenomenon, but the Love wave will not.

The model (Fig. 1) is divided into two parts: one is the SAW generation region, and the other is the fluid region. The first part consists of a 54° Y - X LiNbO_3 substrate with a high electromechanical coupling coefficient and EWC IDTs made of Al material. The 54° Y - X LiNbO_3 substrate bottom boundary is fixed, the top boundary is free (except for the boundary in contact with the IDT), and perfect matching layers are added to the left and right boundaries. The voltages of $V = V_0 e^{i\omega t}$ and $V = 0$

are alternately applied to the odd and even numbers of fingers of EWC IDTs, and the edge effects of the EWC IDTs are ignored during the simulation. The displacement and stress distributions of the substrate are calculated in the frequency domain.

The second part is the microfluidic channel made of PDMS. Since the time difference between the acoustic field and the acoustic streaming field to reach the equilibrium state is several orders of magnitude, based on perturbation theory [38], the acoustic field and the acoustic streaming are defined as first-order and second-order fields, respectively, and they are computed in the frequency domain as well as under steady state studies. The first-order fields are assumed to have a harmonic time dependency with the factor of $e^{i\omega t}$, where $\omega = 2\pi f$ is the angular frequency and i is the imaginary unit. When the SAW propagating in the solid meets the fluid, it will be strongly coupled and radiate longitudinal waves into the fluid. Therefore, the velocity, displacement, and normal stress continuity conditions are applied between the fluid and the piezoelectric substrate boundaries. In the second-order field, due to the existence of the pressure gradient, the acoustic streaming phenomenon is induced. Therefore, when simulating the acoustic streaming phenomenon, the volume force term ($-\nabla \cdot \langle \rho_1 \mathbf{v}_1 \rangle + \rho_0 \langle \mathbf{v}_1 \cdot \nabla \mathbf{v}_1 \rangle$) and mass source term ($\langle \rho_1 \partial \mathbf{v}_1 / \partial t \rangle$) need to be added to the fluid, and the average value of P_2 needs to be 0. For the second-order field, the no-slip boundary condition is imposed on the Lagrangian velocity of the fluid at the fluid–solid interface; the Lagrangian velocity is defined as the summation of the Eulerian streaming velocity $\langle \mathbf{v}_2 \rangle$ and the Stokes drift [39–41]

$$\mathbf{v}_{SD} = \left\langle \left(\int dt \mathbf{v}_1 \cdot \nabla \right) \mathbf{v}_1 \right\rangle. \quad (11)$$

The boundary of the channel in contact with the fluid satisfies

$$\mathbf{v}_2 = -\mathbf{v}_{SD}. \quad (12)$$

The above derivation is meaningful only as long as the perturbation theory is valid and as long as the streaming remains laminar.

2.4. Verification of grid convergence

In order to verify the correctness of the solutions, the grid-convergence analysis is performed. The solutions are compared for decreasing grid size Sz/Wz (Sz represents the maximum grid size in the solution domain, and Wz is a parameter to control the grid size) to determine the point at which the solution becomes independent of any further decrease in Sz/Wz . In the process of removing NSB, the acoustic streaming effect is studied, and since the boundary layer does require a very fine grid, the maximum grid size Sz for the boundary layer region and fluid solution domains is $\lambda/100$,

respectively. The grid convergence parameter $C(\mathbf{F})$ is a relative convergence parameter of the solution \mathbf{F} relative to the reference solution \mathbf{F}_{ref} . The reference solution \mathbf{F}_{ref} is obtained with the maximum value of Wz . The grid convergence parameter is defined as [42]

$$C(\mathbf{F}) = \sqrt{\frac{\int dx dy (\mathbf{F} - \mathbf{F}_{ref})^2}{\int dx dy \mathbf{F}_{ref}^2}}. \quad (13)$$

Note that equations (12) and (13) represent the response of the fluid to the harmonic components of the applied acoustic wave.

In this paper, \mathbf{F}_{ref} is the physical field generated by the fine grid of $Wz = 6$. The effects of the numerical parameter Wz on the first-order field and the second-order field are studied. The grid convergence analysis results are shown in Fig. 2. It can be seen that when $Wz = 3$, all the results remain at $C < 0.005$, which gives satisfactory convergence behavior.

3. Forces on non-specific binding particles

The pollutants are adsorbed on the sensor surface by the van der Waals force and electric double-layer force, resulting in NSB. When the removal forces generated by the acoustic wave are greater than the van der Waals force and the electric double-layer force, NSB can be effectively removed. The removal forces can be divided into linear force and nonlinear force. The SAW force (\mathbf{F}_{SAW}) is a nonlinear force, and the lift force (\mathbf{F}_L) and drag force (\mathbf{F}_D) are linear forces. The directions of these forces are shown in Fig. 3.

3.1. Van der Waals force and electric double-layer force

The main adhesion forces acting on NSB particles immersed in liquids are the van der Waals and electric double-layer forces [43], and the magnitude of these two forces is related to the volume of the particles. Assuming the particle is a sphere of radius R , and at the free surface, the van der Waals force on the particle can be expressed as $F_V \simeq BR/(6y^2)$, where B is the Hamaker constant and y is the distance of the particle from the sensor surface [44]. When calculating the van der Waals force of a particle immersed in a fluid, the value of the Hammark constant is generally taken to be 10^{-20} i. As y increases, the van der Waals force on the NSB particles tends to decrease, so y takes a value of about 0.2–0.4 nm [43]. The surface contact potential generated between two different materials induces surface charge accumulation because of the different local energy state of each material. This leads to the formation of a double-layer charged region around the particle to maintain charge neutrality, thereby generating electrostatic attraction, which can be ignored when the effective diameter of the particle is

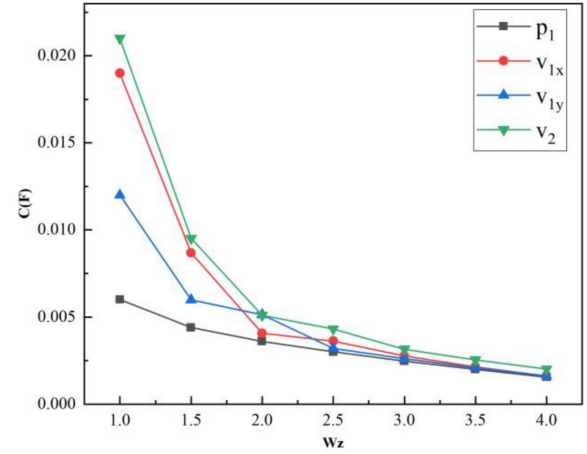


Fig. 2. The relationship between the convergence parameter $C(\mathbf{F})$ of the physical field and the grid control parameter Wz .

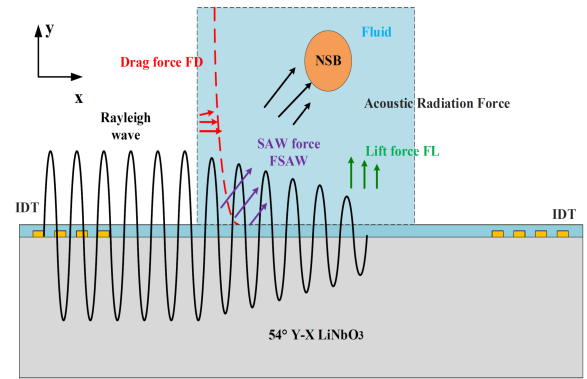


Fig. 3. Schematic diagram of the removal of NSB by SAW.

greater than $5 \mu\text{m}$. For sub-micrometer-sized particles, it is found that the electrical double-layer force and van der Waals force are of the same order of magnitude [44]. In the process of removing NSB particles, it is usually sufficient to consider only the van der Waals force (F_V) [45].

3.2. Lift and drag forces

The lift force (\mathbf{F}_L) and drag force (\mathbf{F}_D) have different effects on the removal of NSB particles. In fact, \mathbf{F}_L can prevent the removed NSB particles from falling back to the sensor surface again, and \mathbf{F}_D can move the NSB particles away from the sensor surface. The directions of \mathbf{F}_L and \mathbf{F}_D are shown in Fig. 3. Based on Bernoulli's equation, \mathbf{F}_L can be estimated from the pressure difference between the bottom and top of the particle as $\rho(\mathbf{v}_2 R)^2$, where \mathbf{v}_2 is the normal velocity of the acoustic streaming. In fact, \mathbf{F}_D is caused by the interaction between the acoustic streaming and the particles, and it is expressed as $\mu R u_2$, where u_2 is the tangential

velocity of the acoustic streaming. It can be seen from the expressions of \mathbf{F}_L and \mathbf{F}_D that their values are proportional to the velocity of the acoustic streaming.

3.3. Acoustic radiation force

When particles are suspended in a fluid and exposed to a traveling wave acoustic field, they experience a time-averaged acoustic radiation force (\mathbf{F}_{TART}), which can be expressed as [46]

$$F_{TART} = \pi a^2 Y_T \langle E \rangle, \quad (14)$$

where Y_T is the acoustic radiation force coefficient, $\langle E \rangle$ is the average energy density of the incident wave, and a is the radius of the spherical particle. Therefore, for the same size of particles in an acoustic field of the same energy intensity, the acoustic radiation force is proportional to Y_T . This coefficient is defined as

$$F = \frac{x^2}{2} \frac{\rho}{\rho^*} \frac{\frac{x_1 j_n'(\kappa_1)}{x_1 j_n'(\kappa_1) - j_n(\kappa_1)} - \frac{2n(n+1)j_n(\kappa_2)}{(n+2)(n-1)j_n(\kappa_2) + x_2^2 j_n''(\kappa_2)}}{x_1^2 \frac{\frac{\sigma}{(1-2\sigma)j_n(\kappa_1)} - j_n''(\kappa_1)}{x_1 j_n'(\kappa_1) - j_n(\kappa_1)} - \frac{2n(n+1)(j_n(\kappa_2) - x_2 j_n'(\kappa_2))}{(n+2)(n-1)j_n(\kappa_2) + x_2^2 j_n''(\kappa_2)}}, \quad (18)$$

where ρ^* , ρ , and σ are the particle density, fluid density, and Poisson's ratio of the particle material, respectively. The parameters κ_1 and κ_2 are defined as

$$\kappa_1 = k_1 a = \frac{2\pi f a}{c_l}, \quad (19)$$

$$\kappa_2 = k_2 a = \frac{2\pi f a}{c_s}, \quad (20)$$

$$k_1 = k a = \frac{2\pi f a}{c_0}, \quad (21)$$

where k_1 and k_2 are the wave vectors of the compression and shear acoustic waves in the particle material, respectively; k is the wave vector of the compression waves in the fluid; c_l , c_s , c_0 , and f are the velocities of the compression and shear acoustic waves in the particle material, the velocity of the acoustic waves in the fluid, and the frequency of the acoustic waves, respectively.

When the Rayleigh wave meets the fluid, it converts into the leaky wave, which radiates into the channel in the form of the longitudinal wave at the Rayleigh angle, so the acoustic radiation force acting on the particle can be decomposed into the normal \mathbf{F}_n and horizontal \mathbf{F}_s components. The expressions are as follows

$$F_n = F_{TART} \cos(\theta), \quad (22)$$

$$F_s = F_{TART} \sin(\theta), \quad (23)$$

$$\sin(\theta) = \frac{c_0}{v_R}. \quad (24)$$

$$Y_T = \sum_{n=0}^{\infty} -\frac{4(n+1)}{k_1} (\alpha_n + \alpha_{n+1} + 2\alpha_n \alpha_{n+1} + 2\beta_{n+1} \beta_n), \quad (15)$$

and α_n and β_n are given, respectively, as

$$\alpha_n = -\frac{(F_n j_n(\kappa) - \kappa j_n'(\kappa))^2}{(F_n j_n(\kappa) - \kappa j_n'(\kappa))^2 + (F_n y_n(\kappa) - \kappa y_n'(\kappa))^2} \quad (16)$$

and

$$\beta_n = -\frac{(F_n j_n(\kappa) - \kappa j_n'(\kappa))(F_n y_n(\kappa) - \kappa y_n'(\kappa))}{(F_n j_n(\kappa) - \kappa j_n'(\kappa))^2 + (F_n y_n(\kappa) - \kappa y_n'(\kappa))^2}. \quad (17)$$

Here, $j_n(\kappa)$ and $y_n(\kappa)$ are the n -order spherical Bessel functions of the first and second kind, respectively. The scattering coefficient F is given by the following equation [46]

Similarly, when particles are suspended in a fluid and exposed to a standing wave acoustic field, they also experience the time-averaged acoustic radiation force (\mathbf{F}_{SART}), which can be expressed as

$$F_{SART} = \pi Y_S \langle E \rangle a^2 \sin(2kx). \quad (25)$$

In (25), Y_S is the acoustic radiation force coefficient in the standing wave acoustic field, $\langle E \rangle$ is the average energy density of the standing wave field, a is the radius of the spherical particle, $k = 2\pi/\lambda$ is the wave number (λ — acoustic wavelength), and x is the distance from the pressure node. The coefficient Y_S is expressed as

$$Y_S = \frac{1}{k_1^2} \sum_0^{\infty} (n+1)(-1)^{n+1} k_1^2 \times (\beta_n(1+2\alpha_n) - \beta_{n+1}(1+2\alpha_n)). \quad (26)$$

The expressions of the normal and tangential acoustic radiation forces in the standing wave field can be written as

$$F_n = F_{SART} \cos(\theta), \quad (27)$$

$$F_s = F_{SART} \sin(\theta). \quad (28)$$

3.4. Acoustic surface wave force (\mathbf{F}_{SAW})

Under the action of the leakage wave, the fluid particle produces displacement components u_y and u_z in the normal and tangential directions, respectively. The expressions for u_y and u_z are shown as

$$u_y = A \exp(i\omega t) \exp(-ik_L y) \exp(-\alpha k_L x), \quad (29)$$

$$u_x = -iA\alpha \exp(i\omega t) \exp(-ik_L y) \exp(-\alpha k_L x), \quad (30)$$

where A represents the amplitude of the SAW, ω represents the angular frequency of the acoustic wave, k_L is the wave number of the leakage wave, and α represents the attenuation coefficient.

The velocity of a fluid particle is the partial derivative of displacement with respect to time. It consists of two terms; the first term varies with the direction of propagation z as $\exp(-\alpha z)$, and the other term varies with z as $\exp(-\alpha bz)$, where $b = \sqrt{2\mu/(\rho_0\omega)}$, and μ is the shear viscosity of the fluid. The second term is neglected when solving for the acoustic streaming force. The viscous boundary layer of water has a thickness of approximately $0.02 \mu\text{m}$ when the frequency of approximately 100 MHz of the removal device is used. Therefore, bz is much greater than 1, and it is reasonable to ignore the second term [47]. The sum of the mass source term ($\langle \rho_1 \partial \mathbf{v}_1 / \partial t \rangle$) in (9) and the volume force term ($-\nabla \cdot \langle \rho_1 \mathbf{v}_1 \rangle + \rho_0 \langle \mathbf{v}_1 \cdot \nabla \mathbf{v}_1 \rangle$) in (31) can be further simplified as $(\rho_0 \langle \mathbf{v}_1 \cdot \nabla \mathbf{v}_1 \rangle + \rho_0 \langle \mathbf{v}_1 \cdot \nabla \cdot \mathbf{v}_1 \rangle)$. Now, F_{SAW} can be written as $(\rho_0 \langle \mathbf{v}_1 \cdot \nabla \mathbf{v}_1 \rangle + \rho_0 \langle \mathbf{v}_1 \cdot \nabla \cdot \mathbf{v}_1 \rangle)R^2$, with R being the radius of the pollutant particle. The direction of \mathbf{F}_{SAW} shown in Fig. 3 can be decomposed into the tangential F_z and the normal F_y components. When the \mathbf{F}_{SAW} force acting on an NSB particle is greater than the van der Waals force, the NSB particle is peeled off from the sensor surface. The tangential and normal components of \mathbf{F}_{SAW} are shown as

$$F_y = -\rho_0(1 + \alpha_1^2)A^2\omega^2 k_i e^{2(k_i y + \alpha_1 k_i x)R^2}, \quad (31)$$

$$F_x = -\rho_0(1 + \alpha_1^2)A^2\omega^2 \alpha_1 k_i e^{2(k_i y + \alpha_1 k_i x)R^2}, \quad (32)$$

where $\mathbf{F}_{SAW} = \sqrt{(F_x^2 + F_y^2)}k_i$ is the imaginary part of k_L and $\alpha = i\alpha_1$, and R is the radius of the NSB particle. The wave number of the leakage wave k_L is a complex number. Its imaginary part k_i represents the extent to which the acoustic wave is dissipated in the fluid. The dispersion equation of the acoustic wave is shown as

$$\left(2 - \frac{q^2}{b^2}\right)^2 - 4\sqrt{1 - \frac{q^2}{a^2}}\sqrt{1 - \frac{q^2}{b^2}} - i\frac{\rho}{\rho_s} \frac{q^4}{b^4} \sqrt{\frac{1 - \frac{q^2}{a^2}}{\frac{q^2}{c^2} - 1}} = 0, \quad (33)$$

which can be solved to obtain the wave number of the leakage wave k_L [48]. In (33), $q = \omega/k_L$, and ω is the angular frequency of the leakage wave; $a = \sqrt{(\lambda + 2\mu_S)/\rho_s}$ and $b = \sqrt{(\mu_S/\rho_s)}$ are the velocities of the longitudinal and transverse waves in the piezoelectric material; λ and μ_S are the Lamé coefficients; ρ and ρ_s are the densities of the fluid and piezoelectric substrate, respectively.

Piezoelectric materials are anisotropic, so different cut piezoelectric materials have different acoustic velocities.

4. Results and discussion

4.1. Effect of surface acoustic wave frequency on removal of NSB

From (29)–(32), it can be seen that the magnitude of the SAW force is related to the intensity and frequency of the acoustic wave. Based on the law of conservation of energy, when the excitation power of the SAW is constant, the higher the frequency of the acoustic wave, the lower the amplitude of it. The direction of the acoustic radiation force on the NSB particle is the same as that of the SAW force, but the role of the acoustic radiation force in the removal process is unknown. In this section, the SAW force and the acoustic radiation force are calculated by applying the same power of the SAW. Then, the role of the acoustic radiation force in the removal process is determined.

From (14)–(18), it can be seen that the acoustic radiation force coefficient Y_T and Y_S are functions of particle mechanical properties and acoustic frequency. Therefore, Y_T and Y_S of particles of different materials will be calculated, so that the optimal frequency for removing different types of NSB particles can be determined. Spherical polystyrene (PS) and PMMA particles are used to simulate different NSB particles, and the relationships between Y_T , Y_S , and k_1 are shown in Fig. 4. In a traveling wave system, when $k_1 < 1$, Y_T is monotonically increasing, but is very small and approximately negligible; it indicates that there is no significant response to acoustic waves for the particles. When $k_1 > 1$, Y_T becomes non-negligible, and it does not show a monotonous increasing trend, but exhibits successive peaks (maxima) and dips (minima) resulting from the free vibration resonance of the NSB spherical particles. Therefore, the response of NSB particles with $k > 1$ to acoustic waves is more significant. In the standing wave system, when $k_1 < 1$, Y_S is much larger than Y_T in the traveling wave system; it indicates that the acoustic radiation force acting on the NSB particles is also very significant in the low-frequency range. When $k_1 > 1$, Y_T and Y_S are not monotonous, but Y_T is always greater than zero, while Y_S is not, which means that the direction of the acoustic radiative force changes with k_1 . The particles in the standing wave field are moved to the pressure node or pressure anti-node under the action of the acoustic radiation force. When the NSB particles are removed from the sensor surface, the movements of the NSB particles are dominated by the acoustic radiation force, under which the NSB particles are refocused to a pressure node or pressure anti-node near the bottom of the channel. Therefore, the removal system based on traveling SAW has more advantages than the standing SAW.

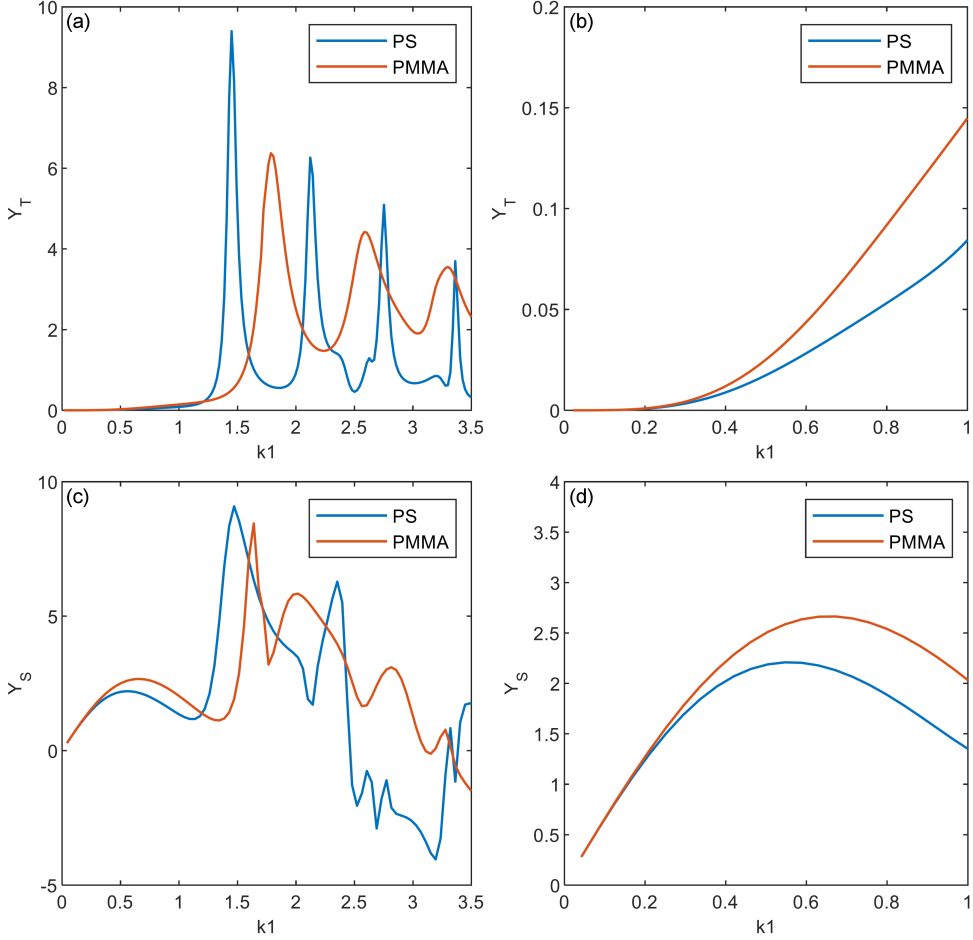


Fig. 4. The relationships between Y_T , Y_S , and k_1 of NSB particles. (a) Y_T in the traveling wave field, (b) enlarged view of k_1 ranging from 0 to 1 in panel (a). (c) Y_S in the standing wave field, (d) enlarged view of k_1 range from 0 to 1 in panel (c).

In the traveling SAW system, the acoustic radiation force of NSB particles is proportional to Y_T . When $k_1 > 1$, even if the size of NSB particles is the same, different types of them have different magnitudes of acoustic radiation force, as shown in Fig. 4a, but the trend of the curves is approximately the same. Therefore, to simplify the discussion, NSB particles in the following refer to PS particles. When $k_1 = 1.45$, Y_T reaches the first peak for PS, so if the radius of NSB particles discussed is $1 \mu\text{m}$, the frequency of 345 MHz of Rayleigh waves can be calculated and used to remove NSB.

NSB can be removed if the resultant force of the acoustic radiation force and SAW force is larger than the van der Waals force. To simplify the discussion, the SAW force is ignored first. When the acoustic radiation force is equal to the van der Waals force, the minimum acoustic field intensity required to remove NSB can be obtained. Based on (14) the van der Waals force ($F_v = BR/(6y^2)$) to which NSB particles of various radii are subjected and the minimum acoustic field intensities required to remove them are determined, as shown in Table I. It can be seen that micron-scale NSB

TABLE I

The van der Waals force experienced by NSB particles with different radii and the minimum acoustic field intensity of the SAW traveling wave with a frequency of 345 MHz required to remove them.

R [μm]	F_n [N]	P_{in} [Pa]
0.01	1.85×10^{-10}	1.63×10^8
1	1.85×10^{-8}	1.19×10^6
5	9.25×10^{-8}	2.30×10^6
7	1.30×10^{-7}	1.60×10^6
10	1.85×10^{-7}	1.36×10^6

particle with a radius of $5 \mu\text{m}$ is difficult to remove, so it is necessary to ensure that the minimum acoustic field intensity in the bottom region of the channel should be greater than 2.30×10^6 Pa. The removal of submicron-scale ($0.01 \mu\text{m}$) NSB particles is also more difficult because the required acoustic field intensity is much greater than that required to remove micron-scale NSB.

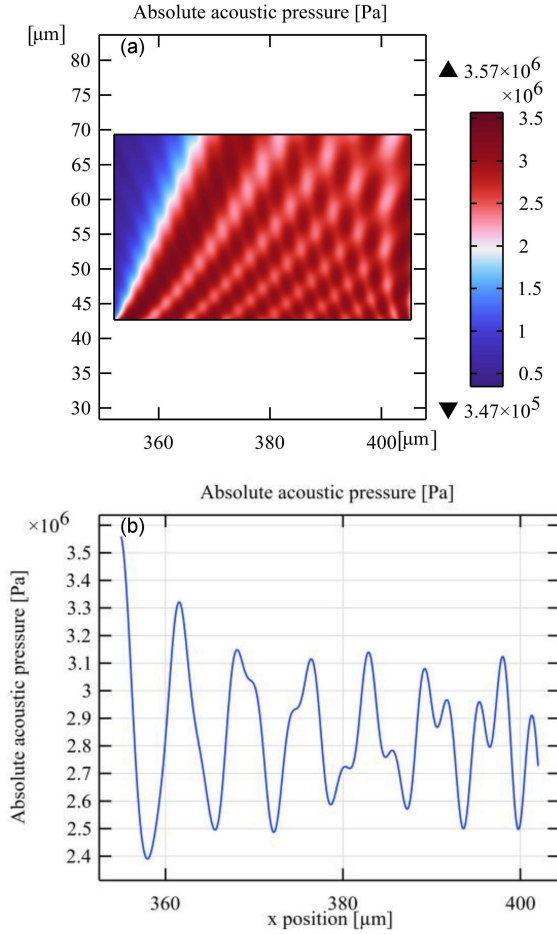


Fig. 5. (a) Acoustic field distribution in the channel. (b) Acoustic field distribution at the bottom of the channel.

TABLE II
Leaky SAW velocity and wavenumber of 345 MHz Rayleigh wave on $54^\circ Y-X$ LiNbO₃ substrate.

Parameter	Value
crystal orientation	$54^\circ Y-X$ LiNbO ₃
Rayleigh velocity [m/s]	3680
leaky velocity [m/s]	$3616 + 62i$
leaky SAW wave number [1/m]	$6 \times 10^5 + 9550i$
attenuation coefficient	2.19

When an electrical signal with a frequency of 345 MHz and a power of 2 W is applied to the bidirectional IDTs to excite Rayleigh waves, the intensity of the acoustic field formed in the channel, as shown in Fig. 5. As can be seen in Fig. 5a, in the horizontal direction, the periodic acoustic pressure field is not formed by wave reflection. This can be explained in terms of Huygens' principle. The acoustic pressure field at any point in a fluid is equal to the sum of infinitesimal spherical wavelets coming from every other point in the fluid domain. Since

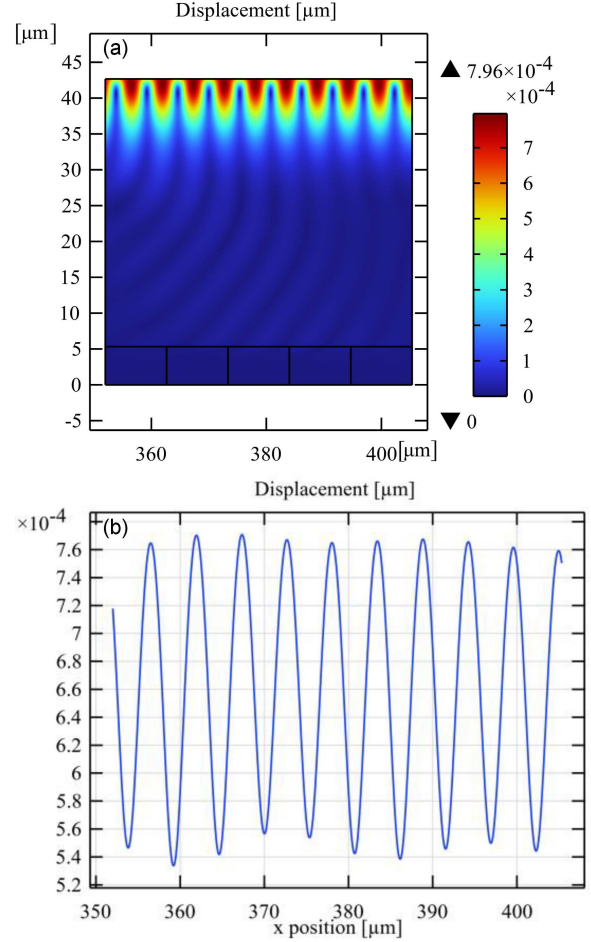


Fig. 6. (a) Displacement distribution of the substrate. (b) Displacement distribution of the substrate surface.

the acoustic waves produced by the spatially limited transducer travel along different propagation paths and experience different phases, they will interfere constructively or destructively at different points of the fluid domain. Consequently, an inhomogeneous acoustic pressure field is formed in the fluid, and the acoustic pressure field distribution is determined by the transducer area defined by the channel size. To sum up, the diffraction of acoustic waves forms the periodicity of the pressure field in the horizontal direction. It can be seen in Fig. 5b that the minimum acoustic field intensity is 2.41×10^6 Pa, so the NSB particles with a radius of 1, 5, 7, and 10 μm are subjected to acoustic radiation forces greater than the van der Waals forces (approximately of the same order of magnitude) and can be peeled off from the surface. However, the NSB particle with a radius of 0.01 μm cannot be removed, and the only way to remove it is to increase the excitation power of the acoustic wave.

The displacement distribution of the substrate is shown in Fig. 6. The minimum displacement of the substrate surface is 5.28×10^{-4} μm. The velocity of the leaky wave is calculated based on (33)

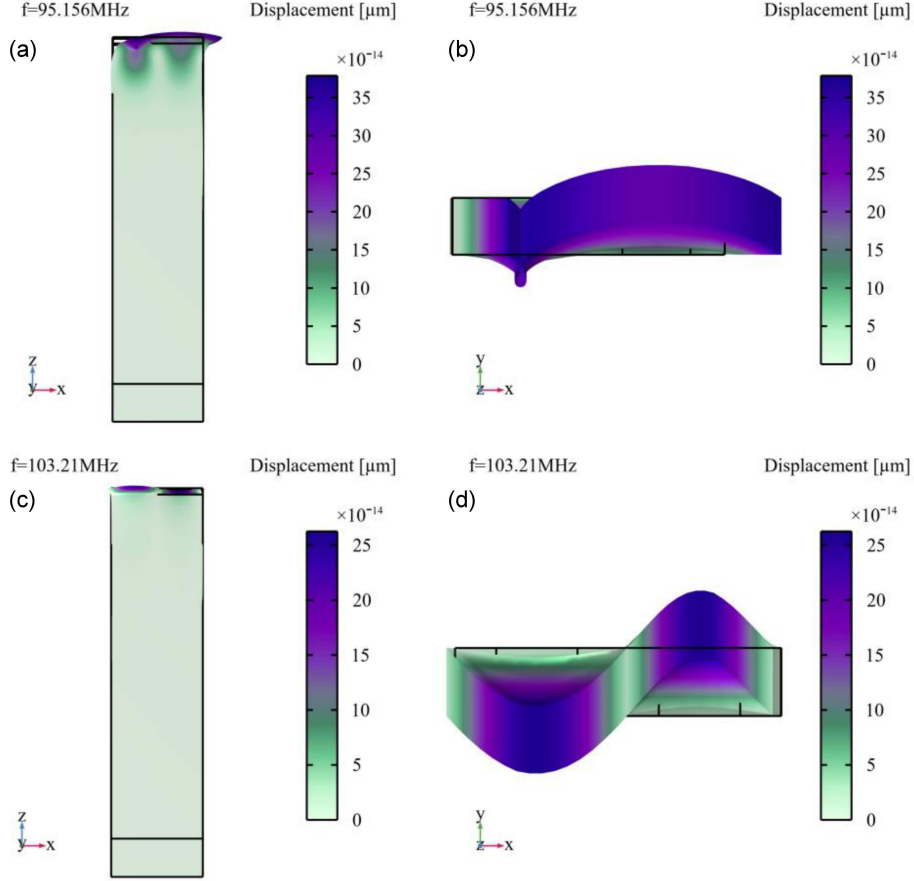


Fig. 7. Mode shape diagram of an acoustic wave. (a) Rayleigh wave mode in the z - x plane. (b) Rayleigh wave mode in the y - x plane. (c) Love wave mode in the z - x plane. (d) Love wave mode in the y - x plane.

TABLE III

Van der Waals force and SAW force on 1, 5, 7, and 10 μm NSB particles in 345 MHz acoustic field.

R [μm]	F_V [N]	F_{SAW} [N]
0.01	1.85×10^{-10}	1.51×10^{-9}
1	1.85×10^{-8}	1.51×10^{-5}
5	9.25×10^{-8}	3.79×10^{-4}
7	1.30×10^{-7}	7.39×10^{-4}
10	1.85×10^{-7}	1.51×10^{-3}

and used to calculate the SAW force, as shown in Table II. The minimum SAW forces on NSB particles with radii of 0.01, 1, 5, 7, and 10 μm are obtained by (31) and (32), as shown in Table III. The SAW force is several orders of magnitude larger than the van der Waals force, while the acoustic radiation force is approximately of the same order of magnitude as the van der Waals force. This means the SAW force is much greater than the acoustic radiation force. So, the acoustic radiation force does not play a dominant role in the removal process. It indicates that the requirement of $k_1 > 1$ does not have to be met, and the frequency of the acoustic

wave can be decreased so that the fabrication cost of the EWC IDT is reduced. However, the amplitude of the SAW force is related to the frequency of the acoustic wave. To ensure the removal of NSB, the frequency should not be too low. So, in this paper, the frequency of 95 MHz of Rayleigh wave is used. For the 54° Y - X LiNbO_3 substrate, when the period of the transducer is 37 μm , the frequencies of the excited Rayleigh and Love waves shown in Fig. 7 are 95 MHz and 103 MHz, respectively.

4.2. Research on removal of NSB particles by Rayleigh wave excited by EWC IDTs

Under a specific excitation voltage, improving the utilization of acoustic waves can enhance the acoustic field intensity in the channel. A unidirectional transducer can generate two oppositely propagating acoustic waves with different intensities, and if it is properly designed, complete unidirectionality can be achieved. Figure 8a shows traditional bidirectional IDTs. Each period consists of two fingers, and the width of the fingers is a quarter of a wavelength. The excitation center of the bidirectional IDTs coincides with the reflection center, which leads to non-directionality. The EWC single-phase

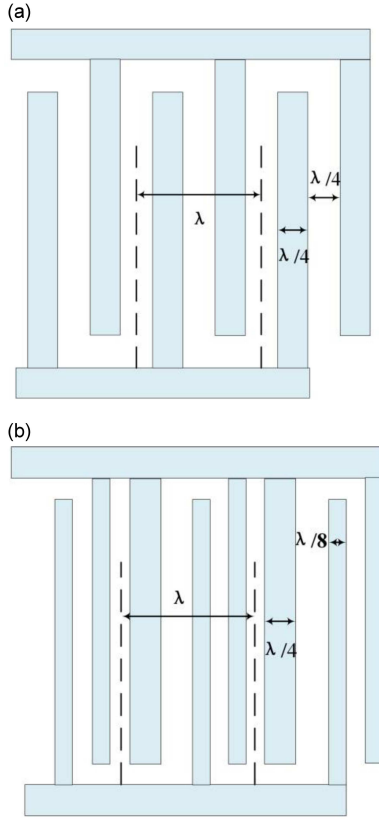


Fig. 8. (a) Bidirectional IDTs. (b) EWC unidirectional IDTs.

transducer shown in Fig. 8b consists of two narrow electrodes with a width of one-eighth wavelength and one wide electrode with a width of one-quarter wavelength per period. The function of the wide electrode is mainly to reflect acoustic waves. The excitation center and reflection center of the EWC unidirectional transducer are not identical, and the unidirectionality is achieved by the reflection of the electrode.

When the EWC transducer shown in Fig. 9a is used to excite the SAW, a voltage is applied to the narrow electrode E2, the center (position B) of which is regarded as the transduction center of the transducer, and electrodes E1, E3, and E4 are grounded. The acoustic wave generated by the transduction center B and that reflected by the narrow electrode E1 cancel each other out, so the narrow electrode E1 has no contribution to the unidirectionality of the transducer. Unlike the narrow electrode E1, the wide electrodes E3 and E4 produce more obvious reflections, so the centers of the wide electrodes E3 and E4 are regarded as the reflection centers (positions A and C, respectively). If the transducer is completely unidirectional, the distance between the transduction center B and the reflection centers A and C must satisfy

$$d = \pm \left(\frac{n}{4} + \frac{1}{8} \right) \lambda, \quad (34)$$

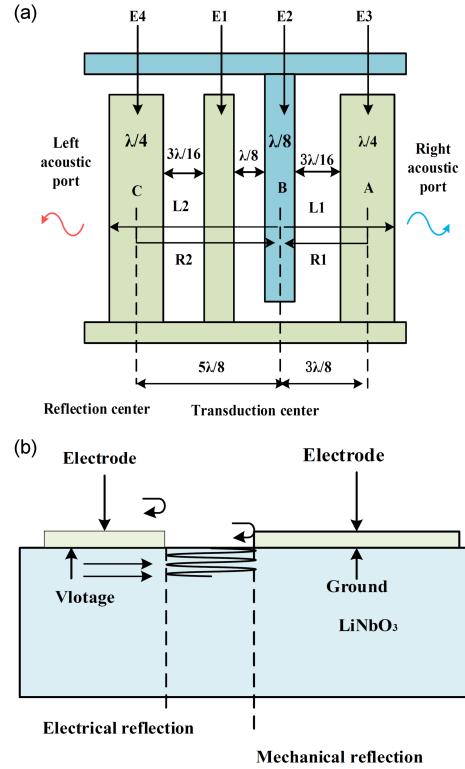


Fig. 9. (a) Excitation and reflection of SAW in EWC transducers. (b) Electrical and mechanical reflections of SAW.

where λ is the wavelength, and d is the distance between the transduction center and the reflection center. If (34) is not satisfied, the unidirectionality of the transducer is not optimal.

Therefore, in the EWC transducer, the distances between the transduction center B and the reflection centers A and C are $3\lambda/8$ and $5\lambda/8$, respectively, as shown in Fig. 9a. The SAWs generated by the transduction center B propagate in two directions (acoustic waves L1 and L2) and are reflected by the reflection centers A and C when encountering the wide electrodes E3 and E4 on both sides. There is a phase difference between the reflected waves R1 and R2 and excited waves L1 and L2. The phase difference mainly consists of two parts. One is caused by the propagation distance, and the other is caused by the electrode reflections. The reflections consist of mechanical reflection and electrical reflection. The impedance discontinuity mainly causes the mechanical reflection, and the electrical reflection is caused by the formation of a constant potential at the interface between the electrode and the LiNbO₃ film, as shown in Fig. 9b. Reflected wave R2 and excited wave L1 interfere destructively because their phase difference is 3π . Similarly, reflected wave R1 and excited wave L2 interfere constructively because their phase difference is 2π . Therefore, the intensity of acoustic waves output by the left acoustic port is greater than the output by the right acoustic port.

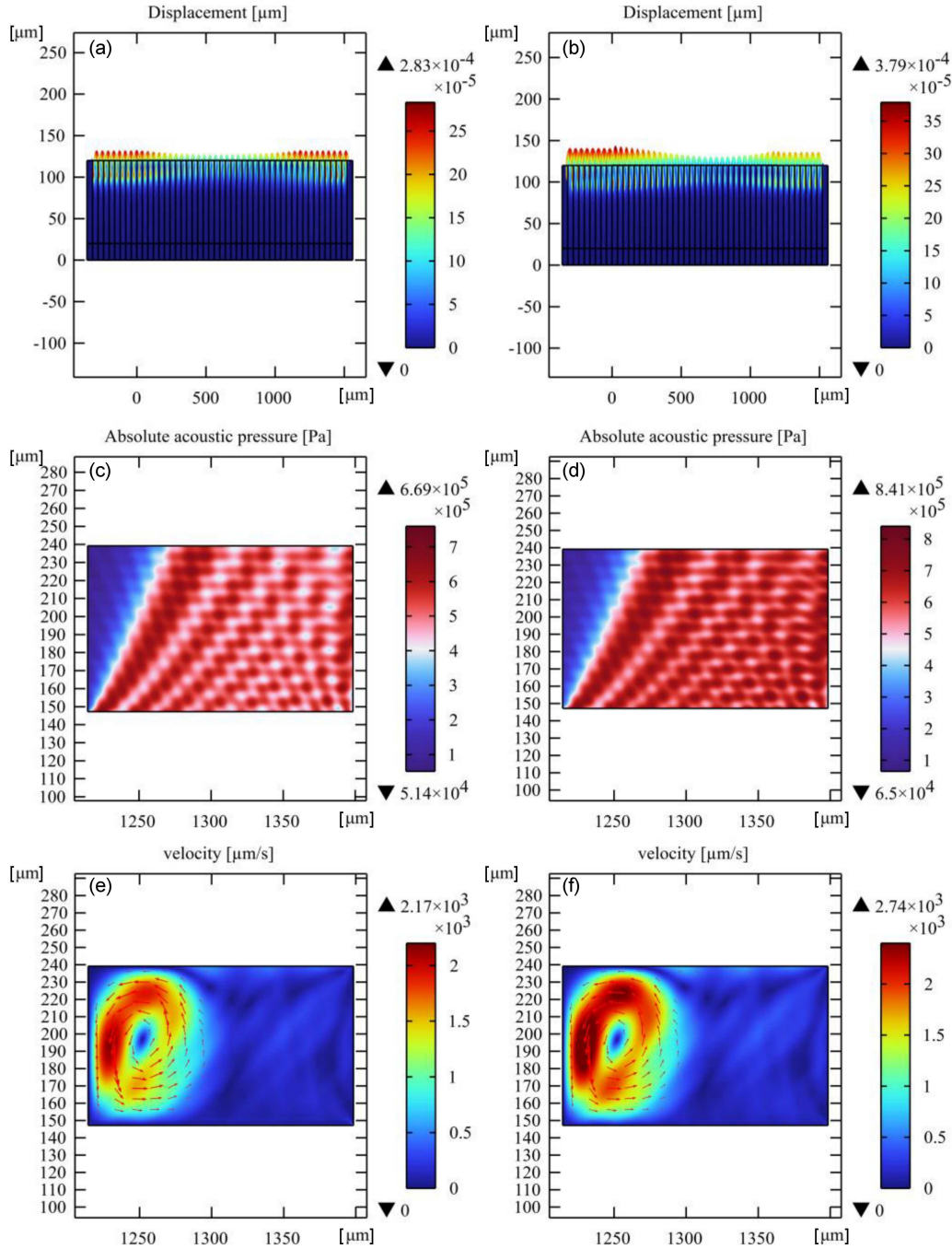


Fig. 10. (a) Displacement of the piezoelectric substrate induced by the bidirectional IDTs. (b) Displacement of the piezoelectric substrate induced by the EWC IDTs. (c) Absolute acoustic field excited by bidirectional IDTs. (d) Absolute acoustic field excited by EWC IDTs. (e) Acoustic streaming induced by bidirectional IDTs. (f) Acoustic streaming induced by EWC IDTs.

In Sect. 4.1, in order to make the acoustic radiation force greater than the van der Waals force, an electrical signal of 2 W is used to excite the SAW. Since the acoustic radiation force plays an auxiliary role in the removal of NSB, in this section, only an electrical signal with a power of 1.2 W is used to explore the advantages of the EWC IDT over the bidirectional IDT. When the period of EWC and bidirectional IDTs is 37 μm , the displacement of

the piezoelectric substrate, the acoustic field, and the acoustic streaming field are shown in Fig. 10. It can be seen in Fig. 10b that the displacement caused by the EWC IDT shows an asymmetry, and the displacement in the left side of the substrate is stronger than that in the right side. This indicates that the SAW propagating to the left is stronger than that propagating to the right. It can be seen in Fig. 10c and d that the intensity of the acoustic

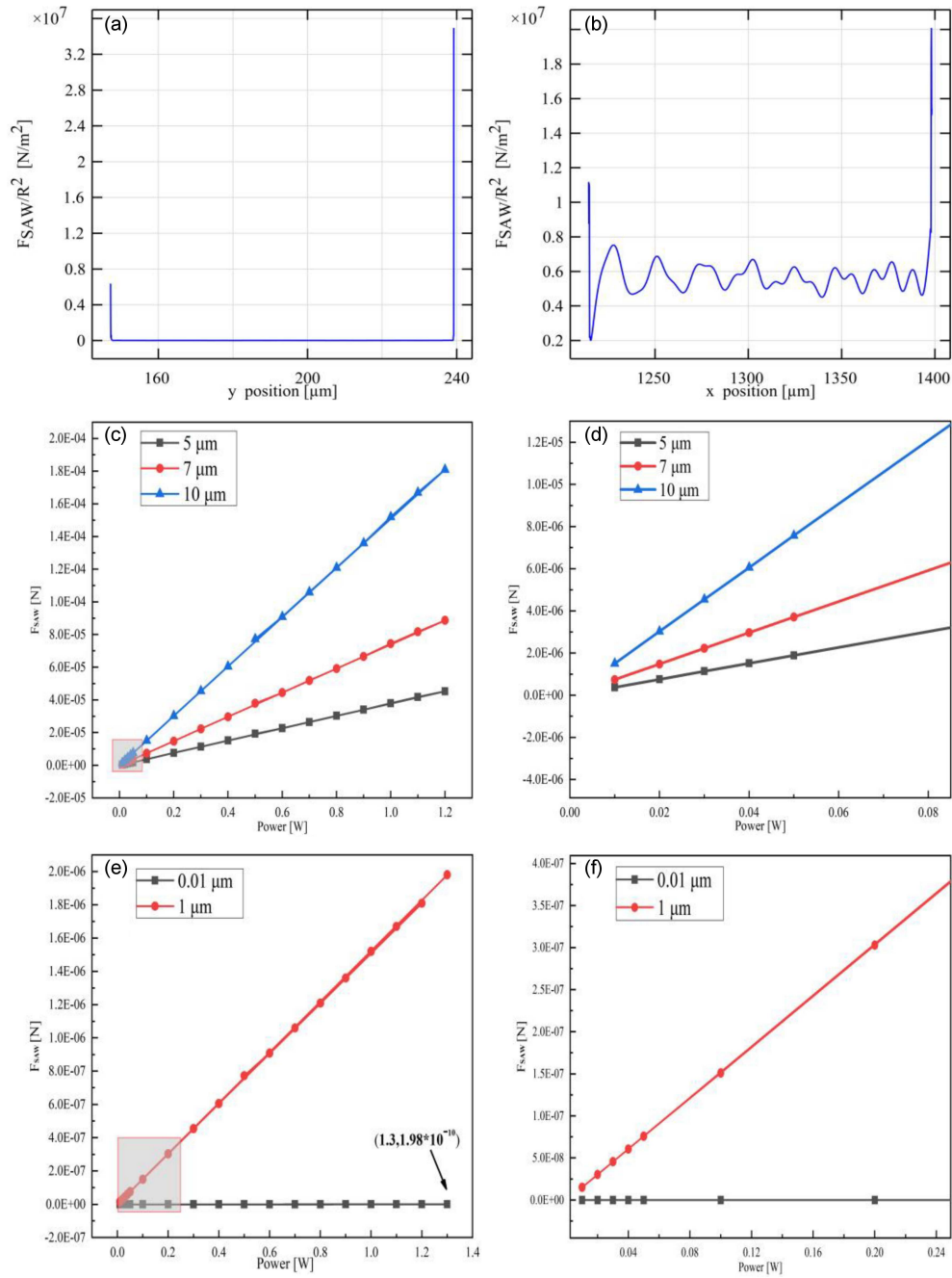


Fig. 11. (a) Distribution of SAW force factor (SAW force/radius²) in the direction of the channel height. (b) Distribution of SAW force factor at the bottom of the channel. (c) Minimum SAW force at the bottom of the channel for 5, 7, and 10 μm radius NSB at different powers. (d) Partial enlarged view of panel (c). (e) Minimum SAW force at the bottom of the channel for 0.01 and 1 μm radius NSB at different powers. (f) Partial enlarged view of (e).

field formed by the bidirectional IDT is lower than that of EWC IDT, but the acoustic field distribution is nearly the same in the channel. Figure 10e and f shows that the acoustic streaming induced by EWC is stronger, but the steaming field distribution is also nearly the same. To sum up, EWC IDT can reduce the bidirectional loss and improve the utilization of acoustic waves, so EWC IDT is applied to horizontal-type SAW devices in the paper.

In the process of removing NSB, the SAW force plays a dominant role. When the input power of EWC IDTs is 1.2 W, the distribution of the SAW force in the channel is shown in Fig. 11. Figure 11a shows the SAW force factor in the channel height direction. It takes the maximum value in the viscous boundary layer at the bottom and top of the channel and decays rapidly when away from the boundary layer. Figure 11b shows the SAW force factor on

the top boundary of the viscous boundary layer at the bottom of the channel. The periodicity of the acoustic field in the horizontal direction results in the near periodicity of the SAW force factor.

It can be seen in Fig. 11c and e that when the input power is 1.2 W, the minimum SAW forces experienced by NSB particles with radius of 0.01, 1, 5, 7, and 10 μm are respectively 1.85×10^{-10} , 1.85×10^{-6} , 4.6×10^{-5} , 9.02×10^{-5} and 1.85×10^{-4} N. Micron-scale NSB (1, 5, 7, 10 μm) particles can be easily removed, however, submicron-scale NSB particle (0.01 μm) is more difficult. When the input power is 0.01 W, the van der Waals force is 1.85×10^{-8} N, while the SAW force on 1 μm particles is 1.51×10^{-8} N, which is slightly smaller than the van der Waals force. When the input power is increased to 0.02 W, the SAW forces on the micron-scale NSB particles are greater than the van der Waals force, so the optimal power of 0.02 W is chosen to be applied to the EWC IDTs to remove the micron-scale NSB particles. For submicron-scale NSB particle (0.01 μm), when the input power is 1.2 W, the van der Waals force (1.85×10^{-10} N) is greater than the SAW force (1.51×10^{-9} N). So, the input power should be greater than 1.2 W to remove it, and the power of 1.3 W can be chosen.

5. Mass sensitivity and detection limits of Love wave sensors

Love wave device has a low-speed waveguide layer on the substrate. Most of the wave energy is confined within the waveguide layer, so power consumption is reduced, and the device sensitivity is increased. The thickness of the waveguide layer has a great impact on the performance of the device. The relationship between the S_{21} parameter and the thickness (λ/A , with A being a dimensionless parameter controlling the thickness of the waveguide layer) of the waveguide layer is shown in Fig. 12a and b. The larger the S_{21} value at the resonant frequency, the lower the insertion loss of the device and the more concentrated on the surface are the acoustic waves. As λ/A gradually decreases, the S_{21} value at the center frequency first increases and then decreases. When the thickness of the waveguide layer is $\lambda/12$, S_{21} reaches the maximum value at the resonant frequency. Therefore, the optimal thickness of the waveguide layer is $\lambda/12$.

The Love wave sensor consists of 54° Y-X LiNbO₃ substrate, PMMA waveguide layer, PDMS channel, and bio-sensitive layer. After reacting with solutions containing different concentrations of meningococcal oligonucleotides (0–150 ng/ μL), the obtained S_{11} is shown in Fig. 13a, in which each data point is averaged over three independent simulations, and the corresponding fitting curve is shown in red. It can be seen that the resonance frequency of the Love wave sensor decreases as the concentration of the solution increases. The change

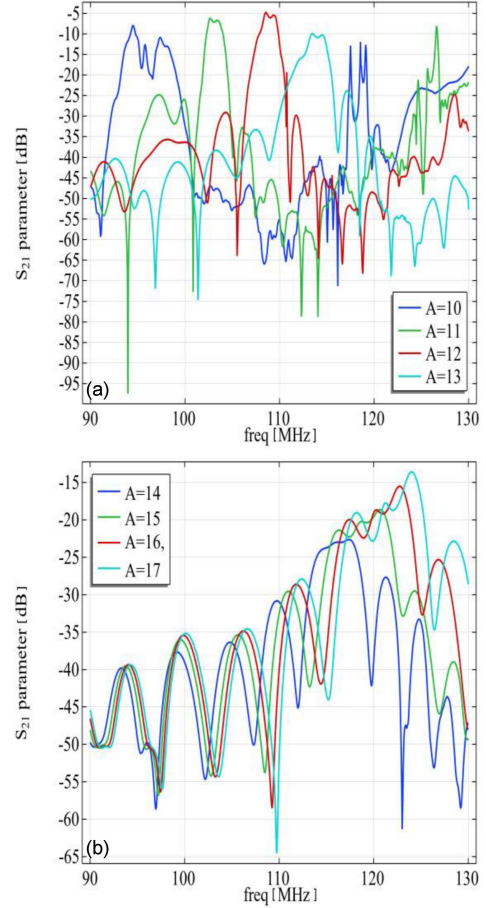


Fig. 12. Effect of waveguide layer thickness on device S_{21} parameters. (a) The thickness of the waveguide layer is $\lambda/13 - \lambda/10$. (b) The thickness of the waveguide layer is $\lambda/17 - \lambda/14$.

in the resonance frequency with the concentration of meningococcal oligonucleotides is shown in Fig. 13b. The resonance frequency is linear in the range of 0–150 ng/ μL , and the magnitude of the frequency shift increases with increasing concentration. At the concentration of 150 ng/ μL , the frequency shift is 50.4 kHz. Therefore, the mass sensitivity of the Love sensor is 336 Hz/(ng/ μL).

The detection limit of the biosensor is given by [49]

$$\text{Limit of detection} = \frac{3 \text{ standard deviation}}{\text{sensitivity}}. \quad (35)$$

Based on (35), the calculated detection limit of the Love wave sensor for meningococcal oligonucleotides is 50 pg/ μL . For the detection of DNA, the detection limit of the Love wave biosensor is lower than SERS, electrochemical impedance spectroscopy, and SPR technologies, but higher than that of ELISA technology, as shown in Table IV (see also [4, 6, 8, 22, 49]). The lower detection limit of the ELISA technology is attributed to the use of high-affinity antigens, as well as antibodies raised against allergies and infections [50].

Comparisons between various biosensors designed for meningococcal detection.

TABLE IV

Sensing technique	Analyte	Sensitivity	Limit of detection	Reference
ELISA	antibodies	–	25 pg/mL	[49]
SERS	DNA	–	317 ng/ μ L	[6]
Electrochemical impedance spectroscopy	DNA	168.64 μ A ng ⁻¹ L/cm ²	5 ng μ L ⁻¹	[4]
SPR	DNA	0.03° (ng μ L ⁻¹) ⁻¹	5 ng/ μ L	[8]
Lamb wave device	DNA	310 Hz/(ng/ μ L)	82 pg/ μ L	[22]
Love wave device	DNA	330 Hz/(ng/ μ L)	50 pg/ μ L	present work

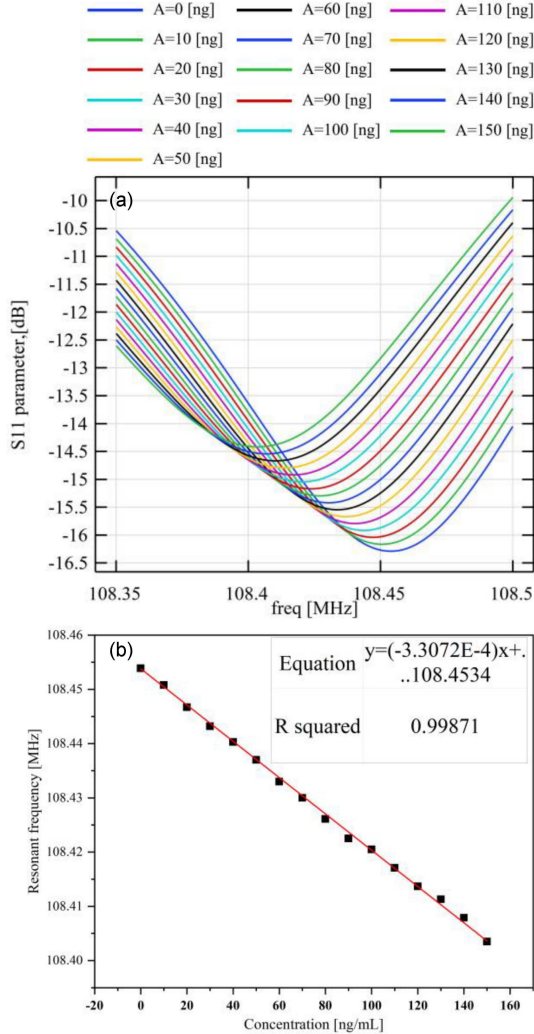


Fig. 13. (a) Changes in the S_{11} curve at different concentrations of meningococcal oligonucleotides solutions. (b) The curve of the resonance frequency of the Love sensor as a function of concentration.

The meningococcal oligonucleotides and the complementary DNA on the bio-sensitive layer are specifically bound in fluid, so the sensing detection should be completed under the condition of fluid loading. The reason is as follows. Firstly, when the meningococcal oligonucleotides solution is completely adsorbed on the bio-sensitive layer, if the fluid is discharged from the channel to detect the meningococcal oligonucleotides, the water

contained in the channel (water adsorbed on the wall, as well as on the surface of the sensitive layer and the detection sample) will have a great impact on the detection results. But in our proposed SAW device, according to Sect. 2.1, when the PBS solution is pumped into the channel in step (i) and step (iii), the respective frequency shifts caused are the same, so the difference between f_1 and f_2 is the result of specific binding of meningococcal oligonucleotides. Secondly, the activity of meningococcal oligonucleotides can be guaranteed. Although the detection limit of the Lamb wave sensor [22] is close to that of the Love wave sensor, the Lamb wave will be strongly coupled with the fluid, and the meningococcal oligonucleotides cannot be detected under the condition of liquid loading, so the application of Lamb sensor is limited. But the Love wave will not strongly couple with the fluid. So, the proposed Love wave biosensor can detect meningococcal oligonucleotides under the condition of liquid loading and is much closer to practical application.

H.L. Cai et al. [50] proposed a SAW biosensor with a gold delay area on LiNbO₃ substrate detecting DNA sequences. An effective biological treatment method for DNA immobilization and abundant experimental verification of the sensing effect have made it a reliable device in DNA detection. Their results indicate that the detection of DNA on the device is repeatable, and the SAW sensor can be recycled. A similar previous study [50] serves as guidelines for our subsequent experimental investigations.

6. Conclusions

In this paper, a portable horizontal-type SAW device based on PMMA/54° Y-X LiNbO₃ is developed to detect meningococcal oligonucleotides and remove NSB particles in real-time. The frequencies of the excited Rayleigh waves and Love waves are 95 MHz and 108 MHz, respectively. The interaction between Rayleigh wave and fluid can remove the NSB from the sensor surface. It is proved that the SAW force plays a leading role in the removal. Love waves do not interact with fluids, and the device based on Love waves is used to detect meningococcal oligonucleotides in response to mass loading. The sensitivity of the Love wave sensor is 336 Hz/(ng/ μ L), and the detection limit is 50 pg/ μ L. If the sensor is used

many times, the adsorption force between the bio-sensitive layer and meningococcal oligonucleotides decreases, which will affect the detection accuracy of the sensor. In this paper, the PDMS channel is designed to bond with the substrate; it is flexible and can be easily replaced by a new one, so the device can be reused. Further research will explore exactly how many times the experiments can be repeated.

The data underlying this article will be shared upon reasonable request to the corresponding author.

Acknowledgments

This research was funded by the National Natural Science Foundation of China, grant number 12264058 and the Program of Science and Technology Plan of Yunnan Province of China, grant number 202301AT070083.

The authors declare no conflict of interest. The funders had no role in the design of the study, in the collection, analyses, or interpretation of data, in the writing of the manuscript, or in the decision to publish the results.

References

- [1] D.B. Go, M.Z. Atashbar, Z. Ramshani, H.C. Chang, *Anal. Methods* **9**, 4112 (2017).
- [2] D.G. Prajapati, B. Kandasubramanian, *Macromol. Chem. Phys.* **220**, 1800561 (2019).
- [3] M. Tak, V. Gupta, M. Tomar, *Biosens. Bioelectron.* **59**, 200 (2014).
- [4] R. Gupta, M.O. Valappil, A. Sakthivel, A. Mathur, C.S. Pundir, K. Murugavel, J. Narang, S. Alwarappan, *J. Electrochem. Soc.* **167**, 107501 (2020).
- [5] K. Gracie, E. Correa, S. Mabbott, J.A. Dougan, D. Graham, R. Goodacre, K. Faulds, *Chem. Sci.* **5**, 1030 (2014).
- [6] M.T. Yaraki, A. Tukova, Y. Wang, *Nanoscale* **14**, 15242 (2022).
- [7] G. Kaur, A. Paliwal, M. Tomar, V. Gupta, *Biosens. Bioelectron.* **78**, 106 (2016).
- [8] A. Ramola, A. Marwaha, S. Singh, *Appl. Phys. A* **127**, 643 (2021).
- [9] N. Chiba, S.Y. Murayama, M. Morozumi, E. Nakayama, T. Okada, K. Ubukata, E. Nakayama, T. Okada, S. Iwata, K. Sunakawa, *J. Infect. Chemother.* **15**, 92 (2009).
- [10] L.D. Saravolatz, O. Manzor, N. VanderVelde, J. Pawlak, B. Belian, *Clin. Infect. Dis.* **36**, 40 (2003).
- [11] X. Wang, M.J. Theodore, R. Mair et al., *J. Clin. Microbiol.* **50**, 702 (2012).
- [12] J. Vuong, J.-M. Collard, M.J. Whaley et al., *PLOS ONE* **11**, e0147765 (2016).
- [13] S. Li, Y. Zhang, J. Tian, W. Xu, *Food Chem.* **324**, 126859 (2020).
- [14] V. Ruiz-Valdepenas Montiel, M.L. Gutierrez, R.M. Torrente-Rodríguez, *Anal. Chem.* **89**, 9474 (2017).
- [15] R. Monošík, M. Stredánský, E. Šturdík, *Food Anal. Methods* **6**, 521 (2013).
- [16] H. Oh, C. Fu, K. Kim, K. Lee, *Sensors* **14**, 21660 (2014).
- [17] D.W. Branch, S.M. Brozik, *Biosens. Bioelectron.* **19**, 849 (2004).
- [18] S. Li, Y. Wan, Y. Su, C. Fan, V.R. Bhethanabotla, *Biosens. Bioelectron.* **95**, 48 (2017).
- [19] J. Ji, Y. Pang, D. Li, X. Wang, Y. Xu, X. Mu, *ACS Appl. Mater. Interfaces* **12**, 12417 (2020).
- [20] H. Wu, H. Zu, J.H.C. Wang, Q. M. Wang, *Eur. Biophys. J.* **48**, 249 (2019).
- [21] W. Wei, W. Zhang, C. Li et al., *Biosens. Bioelectron.* **129**, 231 (2019).
- [22] M. Bharati, L. Rana, R. Gupta, A. Sharma, P.K. Jha, M. Tomar, *Anal. Chim. Acta* **1249**, 340929 (2023).
- [23] J. Nam, W.S. Jang, J. Kim, H. Lee, C.S. Lim, *Biosens. Bioelectron.* **142**, 111496 (2019).
- [24] C.M. Gregory, J.V. Hatfield, S. Higgins, H. Iacovides, P.J. Vadgama, *Sens. Actuators B* **65**, 305 (2000).
- [25] S.K.R.S. Sankaranarayanan, S. Cular, V.R. Bhethanabotla, B. Joseph, *Phys. Rev. E* **77**, 066308 (2008).
- [26] B.G. Loh, D.R. Lee, K. Kwon, *Appl. Phys. Lett.* **89**, 183505 (2006).
- [27] L.A. Kuznetsova, W.T. Coakley, *Biosens. Bioelectron.* **22**, 1567 (2007).
- [28] S.K.R.S. Sankaranarayanan, R. Singh, V.R. Bhethanabotla, *J. Appl. Phys.* **108**, 104507 (2010).
- [29] S. Li, V.R. Bhethanabotla, *Sensors* **19**, 3876 (2019).
- [30] G. Clementi, G. Lombardi, S. Margueron et al., *Mech. Syst. Signal Process.* **149**, 107171 (2021).
- [31] H. Wei, W. Geng, K. Bi et al., *Micromachines* **13**, 329 (2022).
- [32] P.K. Kundu, I.M. Cohen, D.R. Dowling, *Fluid Mechanics* Academic press, 2015.
- [33] J. Lei, F. Cheng, Z. Guo, *Appl. Math. Modell.* **77**, 456 (2020).
- [34] K.A. Naugolnykh, L.A. Ostrovsky, O.A. Sapozhnikov, M.F. Hamilton, *J. Acoust. Soc. Am.* **108**, 14 (2000).

- [35] N. Nama, P.-H. Huang, T.J. Huang, F. Costanzo, *Lab Chip*, **14**, 2824 (2014).
- [36] D. Köster, *SIAM J. Sci. Comput.* **29**, 2352 (2007).
- [37] J.T. Stuart, *J. Fluid Mech.* **24**, 673 (1966).
- [38] K.A. Naugolnykh, L.A. Ostrovsky, O.A. Sapozhnikov, M.F. Hamilton, *J. Acoust. Soc. Am.* **108**, 14 (2000).
- [39] D.G. Andrews, M.E. McIntyre, *J. Fluid Mech.* **89**, 609 (1978).
- [40] O. Bühler, *Waves and Mean Flows* Cambridge University Press, 2014.
- [41] P.B. Muller, R. Barnkob, M.J.H. Jensen, H. Bruus, *Lab Chip* **12**, 4617 (2012).
- [42] J.N. Israelachvili, in: *The Handbook of Surface Imaging and Visualization*, CRC Press, 2022, p. 793.
- [43] C. Xu J. Zhu, *Chem. Eng. Sci.* **60**, 6529 (2005).
- [44] S.K. Sankaranarayanan, R. Singh, V.R. Bhethanabotla, *J. Appl. Phys.* **108**, 104507 (2010).
- [45] T. Hasegawa K. Yosioka, *J. Acoust. Soc. Am.* **46**, 1139 (1969).
- [46] R.M. Moroney, R.M. White R.T. Howe, *Appl. Phys. Lett.* **59**, 774 (1991).
- [47] J. Vanneste, O. Bühler, *Proc. R. Soc. A Math. Phys. Eng. Sci.* **467**, 1779 (2011).
- [48] A.M. Hamad, H.M. Fahmy, W.M. Elshemey, *Radiat. Phys. Chem.* **166**, 108522 (2020).
- [49] M. van der Flier, G. Stockhammer, G.J. Vonk et al., *J. Infect. Dis.* **183**, 149 (2001).
- [50] H.L. Cai, Y. Yang, Y.H. Zhang, C.J. Zhou, C.R. Guo, J. Liu, T.L. Ren, *Biosens. Mod. Phys. Lett. B* **28**, 1 (2014).